Structure and anisotropy of the crust in the Cyclades, Greece, using receiver functions constrained by in situ rock textural data

Élise Cossette[1*], Pascal Audet[1], David Schneider[1], Bernhard Grasemann[2]

1. Department of Earth and Environmental Sciences, University of Ottawa, Ottawa, Canada
2. Department of Geodynamics and Sedimentology, University of Vienna, Vienna, Austria
* Corresponding author: elise.cossette@gmail.com

Keywords: seismic anisotropy, receiver functions, numerical modeling
Word count: ~7770 main text; ~10 390 all; **Tables:** 2; **Figures:** 8

Abstract

Seismic anisotropy data are often used to resolve rock textures and deformation in the crust based on compilations of rock properties that may not be representative of the local geology. In this paper, we use teleseismic receiver functions jointly with in situ rock property data to constrain the seismic structure and anisotropy of the crust in the Cyclades, Greece, located in the back arc region of the Hellenic subduction zone. The receiver function data indicate that the Moho is relatively flat at 25 km depth toward the south and deepens to 33 km in the north, consistent with previous studies, and reveal an intra-crustal discontinuity at depth varying from 3 to 11 km, mostly observed in the south-central Aegean. Harmonic decomposition of the receiver functions further indicates the presence of both shallow and deep crustal anisotropy related to crustal structures. We model synthetic receiver functions based on constraints from in situ rock properties that we measured using the electron-backscatter diffraction technique. Our results indicate that the shallow upper crustal layer is characterized by metapelites with ~5% anisotropy, underlain by a 20 km thick and possibly anisotropic layer of high-pressure rocks comprising blueschist and eclogite and/or restitic crust resulting from magmatism. This study demonstrates the importance of rock textural data in the interpretation of seismic velocity profiles.

Introduction

Seismic anisotropy, the variations of seismic wave propagation with direction, is a powerful tool to study the alignment of minerals in the crust and mantle resulting from large-scale, coherent deformation caused by tectonic processes (e.g., Jolivet et al., 2009; Porter et al, 2011; Endrun et al., 2011). In the upper mantle, seismic anisotropy is generally interpreted as arising from past or current tectonic processes leading to flow-induced crystallographic preferred orientation (CPO) of dry olivine (e.g., Nicolas and Christensen, 1987; Ben Ismaïl and Mainprice, 1998; Jung and Karato, 2001). In the crust, seismic anisotropy can reflect pervasive, fluid-filled cracks or the CPO of anisotropic minerals such as micas. Until recently, the majority of published work on CPO was done using a small number of minerals, in particular olivine, quartz and calcite (Prior et al., 2011), for which we have now a good understanding of their respective CPO development. However, real rocks are rarely monomineralic, and both the modeling of CPO evolution based on these minerals and its relation to observed in situ seismic properties, obtained from seismic waves sampling large volumes of rocks (e.g., crust and/or upper mantle), are problematic. Recent developments in using CPOs to constrain anisotropic seismic properties consider the contribution of all mineral phases in a rock sample and the distribution of rocks in a volume sampled by seismic waves. This approach has been made accessible through the development of the electron backscatter diffraction (EBSD) technique, which measures both single mineral orientation and their distribution in rock samples, and allows the construction of the full elastic tensor for any given rock. This technique now allows a more direct comparison of in situ rock properties to interpret results of seismic anisotropy from observed seismic data.

Coincident with the development in measuring and modeling CPOs using the EBSD technique, seismic investigations using the teleseismic receiver function method are enabling the study of intra-crustal layering at a scale of 1 to 10 km. Notable examples include the heterogeneous and anisotropic structure of the Himalaya-Tibet collisional orogeny (Nábělek et al., 2009), as well as the crustal structure around continental strike-slip fault systems (e.g., Porter et al., 2011; Audet, 2015). These studies provide direct

constraints on the geological and tectonic history of any given area. It has been shown by a few studies (e.g., McDounough and Fountain, 1988; Kern et al., 1993) that laboratory measurements of seismic velocity and anisotropy in rock samples can help interpreting seismic field data; however, no receiver function study to date has used in situ rock seismic properties to interpret or constrain the recovered seismic velocity model.

In a recent paper, Cossette et al. (2015) used textural data from rock samples collected along an exposed crustal-scale detachment zone (the West Cycladic Detachment System, Grasemann et al., 2012) in the Cycladic islands of the Aegean region to study the in situ seismic properties of representative lithotypes. Mineral CPOs were measured using the EBSD technique to derive seismic anisotropy that can then be used to define anisotropic seismic velocity profiles in the region. The aim of this current study is to resolve the structure and anisotropy of the crust in the Cyclades using a combination of seismic data and in situ rock properties from Cossette et al. (2015). We use teleseismic receiver function data from an array of stations in the Aegean Sea to obtain a velocity model of the crust. Receiver functions are first processed using the harmonic decomposition method (Bianchi et al., 2010; Agostinetti et al., 2011; Audet, 2015) to visualize the lateral and vertical continuity of crustal structure and anisotropy across the array. We then calculate synthetic receiver functions based on seismic anisotropy data from Cossette et al. (2015) to reproduce first-order observations that emerge from the receiver functions and harmonic components, and discuss these results in the context of the tectonic evolution of the Aegean region. Our results give insight into the presence of a discontinuity in the upper crust as well as anisotropy layering from the surface to the Moho, and thus suggest a dominant lithologic control on crustal seismic anisotropy in the Aegean region.

Background and setting

The Cyclades form an archipelago in the center of the Aegean Sea (**Fig. 1**), currently the back-arc region of the Hellenic subduction zone resulting from the convergence of the African and Eurasian plates. The tectonic history of this region is characterised by the

NNE-sense of displacement of the African oceanic lithosphere subducting beneath the Aegean lithosphere. The retreating African slab has caused back-arc extension that commenced in the Oligocene and formed the Aegean basin (Gautier and Brun, 1994). The Cyclades were developed during syn- to post-orogenic extension, as Eocene exhumation revealed high-pressure (HP) rocks from deep portions of the collisional zone, and Oligocene-Miocene unroofing was the result of metamorphic core complex formation (MCC; e.g., Lister et al., 1984). Complex kinematics describe the relative motion of the Aegean micro-plate relative to Eurasia: during the middle Miocene, it underwent clockwise rotation in the western Aegean and counter-clockwise rotation in the eastern, whereas the central Aegean behaved as a coherent block (Kissel and Laj, 1988; Walcott and White, 1998). A uniform NNE-SSW stretching lineation is recorded across the Aegean MCCs when restored to pre-Miocene rotation (Morris and Anderson, 1996). The Cycladic islands expose the Attic–Cycladic Crystalline Complex, which classically comprises three geologic units (Bonneau, 1984, and references therein). The lowermost unit is the Paleozoic paragneiss and orthogneiss Cycladic Basement intruded by Triassic granitoids, which is overlain by the Cycladic Blueschist Unit, a polymetamorphic Carboniferous–Permian to latest Cretaceous passive-margin sequence (e.g., Dürr et al., 1978; Blake et al., 1981). Boudins of the blueschist and eclogite assemblages that formed during the Hellenic orogeny are now exposed on Syros and Sifnos islands. The Upper Unit forms various klippen across the Aegean islands with relics of ophiolites, granitoids, Cretaceous metamorphic rocks and unmetamorphosed carbonates (e.g., Reinecke et al., 1982; Altherr et al., 1994; Katzir et al., 1996; Trotet et al., 2001; Skarpelis et al., 2008).

Deformation structures at the microscopic scale such as crystal shape preferred orientations or CPO may give rise to larger scale seismic anisotropy that can be detected using seismological methods. Seismic anisotropy of the crust and mantle in the Aegean has been studied in the last decade using a variety of techniques that have produced a wealth of data. Hatzfeld et al. (2001) studied the shear-wave anisotropy of the upper mantle using the splitting of SKS phases and found that there is significant anisotropy in the north Aegean Sea with a fast axis that aligns with current strain indicators obtained

from GPS measurements, as opposed to fossil strain recorded by surface geological fabric. Evangelidis et al. (2011) complemented this study with separate computation methods and found good correlations between fast anisotropy directions and pre-Miocene stretching lineations of MCCs. A receiver function study by Li et al. (2003) proposed that the presence of 8% anisotropy in the crust could explain the polarity reversal observed on the transverse component at the seismograph station on Santorini island. Surface-wave dispersion measurements (Endrun et al., 2008) suggested spatial variations of radial shear-wave anisotropy (horizontally-polarized S-waves faster than vertically-polarized S-waves) in the Aegean, indicating 4-8% anisotropy in the lower crust. Moreover, layered azimuthal anisotropy has been documented in the upper mantle and the crust (Endrun et al., 2011) by Rayleigh-wave analysis. More specifically, Endrun et al. (2011) suggested that the lower crust in the Cyclades is characterised by 3.5% azimuthal anisotropy, due to an anisotropic fabric corresponding to the direction of Miocene crustal extension. In summary, seismic anisotropy studies of the Aegean consistently show that the lithospheric mantle is characterized by horizontal fast axis aligning with the current extension in the north Aegean, whereas the crust is characterized by fast horizontal axis aligning with Miocene extension in the south. Most of these studies, however, rely on depth-integrated measurements (e.g., SKS splitting, surface-wave dispersion) and cannot resolve anisotropic layering within the crust, or more complex models of seismic anisotropy (e.g., dipping axis of hexagonal symmetry).

Alongside these seismic studies, a textural investigation was conducted by Cossette et al. (2015) describing seismic anisotropy in exhumed rocks along a crustal-scale detachment in the Cyclades. They reported an average of 9.8% and 7.2% of P-wave and S-wave anisotropy, respectively, in upper crustal rocks, and higher values of 20.3% and 12.4%, respectively, in the blueschist assemblages of lower crustal rocks. Their results were well approximated by anisotropy with a slow subvertical axis of hexagonal symmetry (50° to 85° for most samples), which is consistent with strong radial anisotropy and weaker azimuthal anisotropy, with the maximum P-wave velocities also corresponding to the direction of Miocene extension.

Methods

Receiver functions

Receiver functions are calculated for 21 stations in the Aegean, from continental Greece (Athens) to several islands north of Crete (**Fig. 1a**). Two permanent broadband stations of the Geofon (GE) network provided data from 2007 and 2008 to 2014, and the 19 other temporary broadband stations of the EGELADOS (Z3) temporary network provided data from 2005 to 2007. We specifically selected these 21 stations because we have previously reported in situ rock textural data representative of the Cycladic region only (Cossette al., 2015).

A first set of receiver functions was calculated from teleseismic P-waves, using earthquake events with a magnitude M>5.6 occurring at an epicentral distance between 30° and 90° from each station. For the two stations of the GE network (SANT and APE), the dataset was complemented with receiver functions calculated from PP-waves, using events with a magnitude M>6 and epicentral distances between 60° and 130°. The event distribution for the permanent station APE and the temporary station SERI is shown in **Figure 1b** and **c**. Waveform data were extracted 120 s before and after the arrival time of the direct P-wave. Seismograms with signal-to-noise ratio (SNR) lower than 5 dB on the vertical component in the 0.05-1 Hz frequency band were discarded. The horizontal component data were first rotated into radial and transverse components. The vertical and horizontal components were then decomposed into up-going P (compressional), SV (shear radial) and SH (shear transverse) wave modes following Kennett (1991) and Bostock (1998), and using P-wave velocity (Vp) of 6 km/s and S-wave velocity (Vs) of 3.5 km/s, to partially remove the effect of the free surface and isolate the direct P-wave onto a single component of motion. Individual single-event seismograms were then processed to produce receiver functions by deconvolving the P component of motion from both SV and SH components. Deconvolution is performed in the frequency domain using a Wiener filter that takes into account pre-event noise on both vertical and horizontal components to correct for tilting effects (Audet, 2010). Following deconvolution, we further discarded anomalous large amplitude and oscillatory data using

a root-mean-square criterion. The final receiver functions were filtered between 0.1 and 0.5 Hz and stacked into back-azimuth and slowness bins of 10° and 0.002 s/km, respectively.

Receiver functions represent P-to-S converted signals generated from discontinuities in seismic velocity. If the crust were uniform and isotropic with a flat Moho, the receiver functions would show no variation in SV amplitude with back-azimuth, and no energy would be converted onto the SH component. Wherever the receiver functions do display SV amplitude variations with back-azimuth and signal on the SH component, they imply structural heterogeneity (e.g., dipping discontinuity), elastic anisotropy, or both (Cassidy, 1992; Levin and Park, 1997; Savage, 1998; Frederiksen and Bostock, 2000; Audet, 2015). The receiver functions sample anisotropy or structural heterogeneity differently based on the azimuth and incidence angle of the ray path. However, for simple models of heterogeneity (dipping interface) and hexagonal anisotropy with a 45° dipping fast or slow axis of symmetry, we expect to see a 360° periodicity in amplitude with back-azimuth, and a 90° shift between SV and SH amplitudes (Bianchi et al., 2010; Audet, 2015). For anisotropy models involving near-horizontal axis of hexagonal symmetry the patterns are characterized by 180° periodicity, whereas models with near-vertical axis of symmetry produce little variations in back-azimuth due to the near-vertical ray paths of teleseismic P-waves. For intermediate cases of anisotropy with hexagonal symmetry or models with lower elastic symmetry (e.g., orthorhombic), the patterns can be much more complex.

Figures 2a and **c** show the receiver functions for stations APE and SANT, on Naxos and Santorini islands, respectively. Both stations have a back-azimuth coverage that allows direct visualization of radial amplitude variations with back-azimuth. In particular, we observe differences in the arrival time of an early positive arrival (≤1 s) at station APE; between 225° and 325° of back-azimuth, this signal arrives at ~0.5 s, whereas between 325° and 160° it arrives at ~1 s (dashed line in **Fig. 2a**). The transverse component displays polarity reversals at ~0.5 s around 140° and 320° of back-azimuth (black arrows in **Fig. 2a**). The radial component at station SANT also shows variations in arrival times,

for example between 50° and 180° of back-azimuth, where we observe a positive arrival delayed from ~3.5 to ~4.5 s (dashed line in **Fig. 2c**). There is significant energy on the transverse component as well, with several polarity reversals visible at a back-azimuth of 120° (black arrow in **Fig. 2c**). These observations strongly suggest the presence of structural heterogeneity and/or elastic anisotropy in the crust.

P-wave ray angles

Stereonets showing the distribution of P-ray angles at Moho depth (~30 km) were determined in order to see if the receiver functions could resolve the anisotropy in the crust, assuming a P-wave velocity model of the crust estimated from textural data of representative in situ rocks (Cossette et al., 2015). In this case the crust would be characterized by a vertical slow axis of hexagonal symmetry, such that potential horizontal rays would travel at the fast velocity but data with near-vertical rays will sample the slow velocities. Using the ray parameter and the back-azimuth of the teleseismic P-waves used in calculating receiver functions, the corresponding trend and plunge of the rays were calculated and plotted for each station (**Fig. 3**). The P-ray points are concentrated in the center of the stereonet where P-wave velocity is low, with plunges around 60° (incidence angles of ~30°), and would not sample the full directional variability (or anisotropy) in P-wave velocity of the crust. Therefore, the receiver functions would necessarily resolve a seismic anisotropy lower than the total anisotropy.

Migration

Post-processing of receiver functions was performed in order to extract the information on structure and anisotropy of the crust. The receiver functions were first migrated from time to depth using a one-dimensional velocity model (**Table 1**) based on the studies of Bruestle et al. (2012) Makris and et al. (2013) in the Aegean region and on the calculated seismic velocities obtained from Cycladic rocks (Cossette et al., 2015). Since the Cyclades are relatively free of sediments (Makris et al., 2013), P-wave velocities at the surface correspond to those of metamorphic rocks characterised by high values (~6 km/s), and the Moho is located at approximately 30 km depth (e.g., Bruestle et al., 2012; Makris et al., 2013). The P-to-S velocity ratio (Vp/Vs) varies from an upper bound of 1.69 (schist

+ marble + quartzite) and a lower bound of 1.71 (schist + marble + quartzite + blueschist) in the upper crustal section (Cossette et al., 2015) and increases to higher values in the lower crust and mantle (1.74-1.75). We interpolate the Vs and Vp values at an interval of 1 km, and employ the equation of Dueker and Sheehan (1997) to migrate receiver functions over a depth range of 0 to 100 km.

Harmonic decomposition

We jointly analyse the migrated SV and SH receiver functions by decomposing them into back-azimuth harmonics following the method described in Bianchi et al. (2010) and modified by Audet (2015). The harmonic terms are given by:

$$\begin{pmatrix} S_{V_1}(z) \\ \vdots \\ S_{V_N}(z) \\ S_{H_1}(z) \\ \vdots \\ S_{H_N}(z) \end{pmatrix} = \begin{pmatrix} 1 & \cos(\phi_1 - \alpha) & \sin(\phi_1 - \alpha) & \cos(2(\phi_1 - \alpha)) & \sin(2(\phi_1 - \alpha)) \\ \vdots & & & & \\ 1 & \cos(\phi_N - \alpha) & \sin(\phi_N - \alpha)) & \cos(2(\phi_N - \alpha)) & \sin(2(\phi_N - \alpha)) \\ 0 & \cos(\phi_1 - \alpha + \frac{\pi}{2}) & \sin(\phi_1 - \alpha + \frac{\pi}{2}) & \cos(2(\phi_1 - \alpha) + \frac{\pi}{4}) & \sin(2(\phi_1 - \alpha) + \frac{\pi}{4}) \\ \vdots & & & & \\ 0 & \cos(\phi_N - \alpha + \frac{\pi}{2}) & \sin(\phi_N - \alpha + \frac{\pi}{2}) & \cos(2(\phi_N - \alpha) + \frac{\pi}{4}) & \sin(2(\phi_N - \alpha) + \frac{\pi}{4}) \end{pmatrix} \begin{pmatrix} A(z) \\ B_{\parallel}(z) \\ B_{\perp}(z) \\ C_{\parallel}(z) \\ C_{\perp}(z) \end{pmatrix} \quad (1)$$

where the parameter α is described in the following paragraph. In this equation, the sets of SV and SH amplitudes are expressed as sums of cos($k\varphi$) and sin($k\varphi$), where k is the harmonic degree (here k is 0, 1, or 2) and φ is the back-azimuth, at each depth increment. The resulting five harmonic terms (1 for k=0, 2 each for k=1 and k=2) thus represent the back-azimuth variations in the amplitude of SV and SH resolved onto each harmonic degree as a function of depth. The first term A represents the amplitude of the SV signal that does not vary with back-azimuth (k=0); it therefore represents signal originating from background velocity contrasts onto which anisotropy or heterogeneity is superimposed. The two terms B correspond to one periodicity with back-azimuth (k=1) for two orthogonal orientations (B|| and B⊥), and indicate the presence of either a dipping interface or an anisotropic layer with a plunging symmetry axis (Bianchi et al., 2010; Agostinetti et al., 2011; Audet, 2015). The two terms C correspond to two cycles with back-azimuth (k=2) and indicate anisotropy with a horizontal symmetry axis (Levin and Park, 1997; Shiomi and Park, 2008), or azimuthal anisotropy.

In this coordinate system the *k=1* harmonics (B|| and B⊥) would represent signal decomposed into N-S and W-E orientations (Bianchi et al., 2010). Audet (2015) introduced an azimuth α that represents a rotation of the coordinate system defined anti-clockwise from north, for which a particular harmonic component has maximum energy (variance) over a given depth range. Here we search for the value of α that minimizes the energy on the second component (i.e., where the variance is minimal on B||). This azimuth corresponds either to the strike of a dipping interface or to the horizontal orientation of the fast axis of symmetry of an anisotropic medium. The depth range over which the orientation α was determined is from 0 to 30 km depth, roughly corresponding to the Moho. This procedure limits our ability to characterize intra-crustal variations in the orientation of anisotropy, and the recovered azimuth therefore represents the orientation of the dominant source of anisotropy in the crust.

Figure 4 illustrates the relation between SV and SH amplitudes, the harmonic component and α for a model characterized by a shallow anisotropic layer with a dipping slow axis of hexagonal symmetry. Similar arguments can be used to deduce the relation obtained for other models involving hexagonal anisotropy or dipping interfaces (see also Porter et al., 2011).

Figures 2b and **d** show the harmonic decomposition for stations APE and SANT. The terms *A* (*k*=0) correspond to the migrated SV components stacked over all back-azimuths (**Fig. 2a** and **c**), and show the velocity contrasts that do not vary with back-azimuth. On the other components, stronger amplitudes correspond to a preferred orientation (α in this case). For station APE, there is very little energy on the *C* terms, which allows us to discard the presence of anisotropy with horizontal symmetry axis. The energy was minimised on B|| (with an obtained orientation α of 80°), thus the signal is dominantly projected onto B⊥. On Santorini (SANT), the *C* terms contain less energy compared to the A and B terms, again indicating a dipping interface or anisotropy with a plunging axis of wave propagation. Although the variance was minimised on B|| (with an estimated α of 11°), there is still significant energy on this component, and a single trend of symmetry

axis for the entire depth range could not be found. Although the harmonic terms for SANT are ambiguous compared with those for station APE, these results suggest the presence of a dipping layer and/or anisotropy with a plunging axis instead of anisotropy with a horizontal axis.

Results

Receiver functions

Figure 5 shows the radial component receiver functions stacked over all back-azimuths in the time domain and migrated to depth in order to visualize the main features of the data. The positive arrival at ~3 s corresponds to the downward increase in velocity at the crust-mantle interface, which varies between 22.5 to 33 km depth across the array (bold dashed line in **Fig. 5**). Although not shown here, a second positive pulse with similar amplitude is found between 10 and 11 s, followed by a negative arrival at 12-13 s, which correspond to the free-surface reverberations. At ~1 s, a set of positive arrivals can be detected, corresponding to a downward increase in velocity at a depth of approximately 3 to 11.5 km (thin red dashed line in **Fig. 5**). There seems to be an additional negative arrival at ~4.5 s, corresponding to a downward decrease in velocity at depths of 40-50 km (thin blue dashed line in **Fig. 5**). The double positive-negative pulses between ~3 to 4.5 s may indicate a ~10 km high-velocity mantle lid (shaded area in **Fig. 5**) immediately below the Moho, sandwiched between the low velocity crust and underlain by normal velocity mantle. In this paper we focus on results for the crust and ignore deeper structure.

Harmonics

Figure 6 shows the corresponding variations in the five harmonic components, sorted by station location from north to south. The A term (k=0) shows two interfaces with positive velocity contrasts (**Fig. 6a**) identical to the stacks of radial components of the migrated receiver functions (**Fig. 5b**). The shallower discontinuity (thin dashed line in **Fig. 5a**), clearer in the southern part of the profile, appears almost continuously and is found at depths of 3 to 11.5 km. The second discontinuity (Moho; bold dashed line in **Fig. 5a**) is

found at depths varying from 22.5 to 33 km. This discontinuity is better defined under the southern stations (i.e., south-central Aegean), from KEAI to SANT, where it is relatively horizontal (average depth of 25.5 km). Beneath the northern stations, the discontinuity is not as clear and seems to be located a little deeper with a reduced velocity contrast. The uncertainty in the depth estimates of the interfaces varies between 2 to 5 km due to the width of receiver function peaks and the uncertainty in the background one-dimensional velocity model used in the migration.

Figure 6b and **c** show the B|| and B⊥ components, respectively, that reflect periodicities of 360° in back-azimuth. Since we minimise the energy on the B|| component in order to find α, we find insignificant energy on this component, indicating that the anisotropy is coherent within the crustal column. The B⊥ harmonics show features (shaded areas in **Fig. 6c**) that suggest the presence of either dipping interfaces or anisotropic layers that are sub-horizontal in the central and southern parts of the profile and appear to be deepening toward the north. Positive amplitudes are found at a depth of ~50 km toward the north and gently rise up and flatten out at depths of ~32 km (shaded area in red). Just above, we find negative amplitudes with the same shape arriving at depths of ~38 km in the north, rising up and flattening to depths of ~18 km in the central part (shaded area in blue). These amplitudes produce a polarity reversal, best seen in the south-central Aegean, occurring at the same depth as the second discontinuity (bold dashed line in **Fig. 6c**) on the A component (i.e., at 25.5 km depth). Positive amplitudes are also observed at shallow depths, around 5-12 km (thin dashed line in **Fig. 6c**).

The harmonics with k=2 (**Fig. 5d, e**) do not contain significant energy and are comparatively noisy. It is interesting to note, however, that the C⊥ component yields similar patterns as in the B⊥ component, with positive and negative arrivals that are deeper in the north and shallower in the central and southern parts (blue and red shaded areas in **Fig. 6e**).

Interestingly, the azimuths α for which the energy is minimised on the B|| component do not give any consistent orientation (Fig. 6) – rather, they sample orientations between 0° and 180°.

Modeling

The harmonic terms are useful in the visualization of lateral and depth variations in directional properties but provide limited insight into the source of the anisotropy. We therefore attempt to constrain the velocity structure and anisotropy of the crust and mantle by simulating receiver function data. Although we cannot rule out the presence of dipping interfaces based on the results from the previous sections, we focus here on modeling receiver function data using elastic anisotropy for two main reasons. First, if the signal on the B⊥ harmonics were due to dipping interfaces, we would expect the azimuth α to be consistent with the general deepening of the main crustal discontinuities (e.g., **Fig 6a**), which is not the case. Second, there is strong evidence for elastic anisotropy in the crust and mantle from previous seismic studies (e.g., Li et al., 2003; Endrun et al., 2008; Endrun et al., 2011) and from in situ rock textural data (Cossette et al., 2015). Unfortunately the bias introduced from neglecting the effect of dipping interfaces is difficult to estimate, and would require further work.

We generate synthetic receiver functions by modeling plane wave propagation through a stack of homogeneous, anisotropic layers using the reflectivity technique of Kennett (1983) and Thomson (1996). Each layer is defined by its thickness, density and P- and S-wave velocities. Anisotropy is modeled as hexagonal symmetry with either a fast or slow axis of symmetry, and is parameterized by the percent anisotropy and the trend and plunge of the symmetry axis. Parameters used in one-dimensional velocity models are based on seismic properties constrained by in situ rock properties described by Cossette et al. (2015) and structural information (e.g., depth to discontinuities) constrained by the receiver function data. Synthetic receiver functions are calculated at the same back-azimuth and slowness range as the observed data. Each set of synthetic receiver functions is further processed using the harmonic decomposition to compare with the observed

399 harmonic terms. The objective of the modeling is to reproduce the calculated receiver
400 functions using anisotropy information from textural data. We calculate the root-mean-
401 square of the residuals (**Table 2**) between the calculated and synthetic receiver functions
402 over the first 5 s in order to quantitatively evaluate the fit to receiver function data. We
403 also show how adding anisotropy to the velocity models improves the fit with respect to
404 an isotropic model. We perform synthetic modeling of receiver functions at station APE
405 because it has a good back-azimuth coverage and high signal-to-noise ratio, with clear
406 polarity reversals that suggest the presence of anisotropy. The consistency of the
407 harmonic terms (**Fig. 6**) suggests that any model that reproduces the data for station APE
408 can be confidently extended to other stations in the network, with minor adjustments
409 (e.g., depth to crustal interfaces).
410
411 Station APE yields two positive arrivals on the radial component stacks, at depths of ~7
412 km and ~27 km (horizontal red lines in **Fig. 2b**). In order to reproduce these two
413 discontinuities, we tested several models taking into consideration the geology of the
414 Aegean, in order to create two velocity jumps at 7 and 27 km. The lithology of the region
415 comprises blueschist and eclogite rocks from the Cycladic Blueschist unit, which are
416 characterised by faster seismic velocities than the metapelites and marbles and thus
417 appropriate for a velocity increase at 7 km. The tectonic extension that led to the
418 formation of the metamorphic domes in the Aegean only exhumed a small part of these
419 HP rocks. It is likely that we find the same lithotypes at shallow depth, discretely
420 overlying the Cycladic basement composed of schists and orthogneiss (Andriessen et al.,
421 1987). At 27 km depth we expect to reach the Aegean lithospheric mantle and therefore
422 assign mantle values below this interface. Below we present 6 models (**Table 2, Fig. 7**)
423 and describe briefly how the synthetic receiver functions were affected by the variation of
424 specific parameters.
425
426 Model 1 (**Fig. 7a**) is the most simple and is based on the observation of a polarity reversal
427 at 140° and 320° on the transverse component of station APE. In the first layer we use a
428 slow axis of symmetry, as found in most minerals in the upper crust with a hexagonal
429 symmetry approximation (e.g., Lloyd et al., 2009; Erdman et al., 2013), trending 320°

with a plunge of 60° and no more than 10% anisotropy (Cossette et al., 2015). The lithology corresponds to metapelites with seismic velocities calculated from EBSD data (**Table 2**). The second layer has an average of blueschist and eclogite seismic velocities (Bezacier et al., 2010; Cossette et al., 2015), and this layer is isotropic for simplicity. Synthetic receiver functions for this model show positive arrivals at ~1 and ~3 s, similar to calculated receiver functions at station APE (**Fig. 2a**). The amplitude at 1 s is smaller than the one at 3 s, consistent with the observations. On the transverse component of the synthetic receiver functions, the polarity reversals are reproduced at 1 s and at back-azimuths of 140° and 320° (black arrows in **Fig. 7a**), compared with ~0.5 s for the observed data. The general pattern, in particular the negative amplitudes from 2-5 s, between 0° and 140° back-azimuth (dashed box in **Fig. 7a**), also matches the calculated receiver functions. The harmonic decomposition shows that the high velocity layers are located at 7 km and 25 km. There is no energy on B|| (α = 88°) and B⊥ has a positive pulse at ~8 km depth, as in the observed data.

Model 2 (**Fig. 7b**) has the same parameters as Model 1, except for a trend of symmetry axis that is now 140°. The resulting receiver functions show the same radial stack as in Model 1, although the variations in SV amplitude with back-azimuth are different. There is a good match between the synthetic and calculated receiver functions for the positive amplitudes at 0.5-1 s, between 75° and 300° back-azimuth. However, between 300° and 75° back-azimuth, the synthetic receiver functions yield earlier arrival times (black dashed line in **Fig. 7b**). The transverse components show a pattern that does not correspond to the observed one. Even though the polarity reversals occur at the right back-azimuths (black arrows in **Fig. 7b**), they are of opposite sign. The harmonic decomposition allows us to find an azimuth α of 82° when energy is minimised on B||, very similar to the α of 80° at station APE. Although α is very similar, the least square values are higher compared to Model 1 and indicate a poorer fit.

In Model 3 we explored the effect of changing the azimuth of the symmetry axis. We found that increasing the azimuth to 350° yields a better fit to the radial component, but a worse fit to the transverse component. Furthermore, a quite different orientation α of 67°

461 is obtained. When decreasing the azimuth to 310°, the fit to the SV component is much
462 worse, whereas the SH component fit decreases only slightly. We found that an azimuth
463 of 330° was the best estimate (**Fig. 7c**), with an orientation α of 81°, very similar to the α
464 at station APE.
465
466 Varying the anisotropy in the upper crust, in Model 4 (**Fig. 7d**), allowed us to find that
467 the fit to the SV and SH components rapidly decreases with higher values of anisotropy.
468 The best fit was obtained with an anisotropy of 5%; values lower than 5% also lead to a
469 poorer fit.
470
471 Model 5 considers anisotropy in the second layer. Since the seismic anisotropy of
472 eclogite is well approximated with hexagonal symmetry with a slow axis and is very
473 weak (1-4%, Bezacier et al., 2010; Worthington et al., 2013), we first modeled slow
474 anisotropy of 1-3% in the second layer, which gave a poor match between calculated and
475 synthetic receiver functions. On the other hand, we obtained better results when modeling
476 an anisotropy of <5% with a fast axis of symmetry (**Fig. 7e**). The transverse component
477 shows more obvious negative amplitudes between 0° and 100° back-azimuth, at 1.5-2 s
478 (dashed box in **Fig. 7e**), similar to what is found at station APE. Moreover, the fit was
479 better with an azimuth of 320° instead of 330° for the fast axis of symmetry. The
480 harmonic decomposition for this model yields an orientation α of 85°, and the B$\perp$ term
481 now displays a double polarity as found at station APE.
482
483 We made other observations that are not compiled in the table, but are summarised here.
484 Adding a 1 km-thick layer of higher velocity (i.e., 6.5 km/s) at the surface with the same
485 anisotropy (5%) as in the metapelites increases the fit of the SV component with little
486 effect on the SH component. It allows creating the negative amplitudes (dashed circle in
487 **Fig. 7f**) observed at 0-0.5 s on the APE receiver functions and 0-2 km depth on the APE
488 harmonic decomposition (dashed circle in **Fig. 2b**). Using more gentle plunges for the
489 symmetry axis creates a worse match. Steeper plunges attenuate the effect of anisotropy
490 and obliterate the patterns on the transverse component. A thin layer of high anisotropy
491 (10%, which could correspond to very anisotropic blueschist assemblage) just above the

20 km thick layer notably increases the fit of the SV component, and only slightly decreases the fit of the SH component. Model 6 (**Fig. 7f**) is an attempt for a more complex model accounting for these observations and comprising many parameters. It includes a thin layer of high velocity at the surface, 6 km of anisotropic metapelites, 1 km of high anisotropy (with densities and velocities corresponding to blueschist) and 19 km of dense material with a fast axis of symmetry for the anisotropy. This creates the best fit for the radial component while maintaining an acceptable fit to the transverse component relative to the other models.

Discussion

Our results are summarized in Figure 8. The radial component stacks of the receiver functions and the A harmonic terms all point to a discontinuity at 22.5-33 km depth, characterised by a sharp downward velocity increase that likely corresponds to the Moho, with the south-central Aegean showing a relatively flat Moho with an average depth of 25.5 km. Similar Moho depths of 25-29 km have been documented in the northern and central Aegean (Bohnhoff et al., 2001; Tiberi et al., 2001; Li et al., 2003; Tirel et al., 2004; Sodoudi et al., 2006, 2013; Makris et al., 2013). Low crustal thicknesses are likely caused by back-arc extension associated with elevated sub-crustal temperatures. These results are consistent with the thermal isostasy model of Hyndman and Currie (2011) that relates low crustal thickness in back-arc regions to uniformly high elevation in modern Cordilleras that is supported by a hot, buoyant mantle. This model predicts a crustal thickness of ~27 km in back-arcs where the elevation is at sea level (compared to ~38 km in a stable craton at the same elevation), indicating that the mantle beneath the Aegean Sea may be on average 250°C hotter compared to mantle temperatures beneath cratons, from the surface down to ~200 km depth. Moreover, we find the thinnest crust (22.5 km) for the islands of Ios and Naxos, which are high temperature domes. Andros, which only experienced moderate heating during the Eocene (Jolivet and Brun, 2008), has a higher crustal thickness of 29 km and stations AT01, AT03 and AT04, on the continent, also have thicker crusts varying between 27 and 32 km (Figure 8).

523 The harmonics with an order k=1 (in particular, B⊥) give insights into the depth and
524 lateral variations in the anisotropic structure, and show a deepening of a double-polarity
525 pulse from south to north. These signals seem to mirror the ones of the A harmonics,
526 where the Moho appears to be deeper in the north as well, and where it overlaps the
527 double polarity observed on the B⊥ component. The origin of the deepening double-
528 polarity layer to ~50 km depth on the B⊥ component is ambiguous and may represent a
529 north-dipping low-velocity zone or a dipping layer of anisotropic material. However the
530 Hellenic slab is >75 km deep in the southernmost portion of the array, with greater depths
531 toward the north (Li et al., 2003; Sodoudi et al., 2006), thus the double-polarity pulses
532 cannot be directly linked with the subducting crust of the African lithosphere. Moreover,
533 the Aegean Moho is documented to be relatively flat in the Aegean back-arc basin (e.g.,
534 Tirel et al., 2004) and the estimated azimuths α are not consistently oriented with the
535 strike of a single dipping interface. Li et al. (2003) reported that at station SANT, an
536 unlikely dip of 40° of the crust-mantle interface would be needed to resolve the variation
537 in arrival times at the Moho, thus favouring the hypothesis of elastic anisotropy. This
538 suggests the presence of an anisotropic layer rather than a dipping interface, although we
539 cannot rule out the occurrence of dipping layers with our data. Mineral anisotropy is
540 strongly expected due to the presence of pervasive stretching lineations related to ductile
541 flow in the weakened lower crust during the exhumation of metamorphic core complexes
542 in the Cyclades (Jolivet et al., 2013). At the observed depth of the polarity reversal,
543 however, anisotropy would most likely be related to flow in the mantle lithosphere,
544 oriented parallel to the current strain field of extension (Endrun et al., 2011).
545
546 The azimuths α obtained from the minimization of variance on the B|| component
547 represent either the strike of a dipping interface or the orientation of the fast axis of
548 symmetry in anisotropic materials with hexagonal symmetry. Our data yield azimuths
549 ranging between 0° and 360°, suggesting that the trend of the anisotropy is not coherent
550 across the array of stations. However, the apparent scatter may be expected for a sub-
551 vertical axis with very steep plunges, where the trend of the anisotropy axis is more
552 difficult to resolve, indicating that the symmetry axis is dominantly vertical. This is
553 consistent with the study by Cossette et al. (2015), where a slow sub-vertical axis of P-

554 wave velocity was the best approximation for the observed seismic anisotropy. The trend
555 of the slow symmetry axis is obtained by adding 90° to the estimated azimuth α. The
556 harmonic decomposition performed here also corroborates the result of a sub-vertical
557 axis, since a horizontal axis of symmetry would be mostly observed on the *C* component.
558 Finally, the energy still present on the B|| component at some stations after minimizing
559 the variance on this component suggests that there are likely different anisotropic layers
560 with slightly different trends of symmetry axis at various levels within the crust.
561
562 We note that the seismic velocity models are not unique as several models could fit the
563 calculated data almost equally well. These models can become quite complex when
564 defining several layers with many parameters, thus we preferred to focus on the simplest
565 ones. Our models require a thick layer of ~20 km of almost constant and high velocity in
566 order to create two velocity jumps similar to the ones observed at station APE. There is
567 evidence that the Cycladic Basement unit experienced HP metamorphism, later than the
568 HP metamorphic episode of the Cycladic Blueschist Unit (Ring et al., 2001 and
569 references therein), which could explain the presence of dense and high-velocity material
570 beneath the upper crust. Moreover, due to the significant crustal thinning and extension
571 (700 km, Jolivet and Brun, 2008), the Cyclades experienced Miocene magmatism (e.g.,
572 Serifos, Naxos, Tinos, Mykonos islands) and we speculate that partial melting probably
573 resulted in a restitic lower crust, which would have higher seismic velocities since it
574 would be depleted in low-temperature (i.e., lower velocity) minerals like muscovite,
575 potassium feldspar and quartz. However not all stations in the Cyclades require this thick
576 layer of high-velocity material, as shown by the downward velocity decrease around 1.5-
577 2 s (~15 km depth) at station ANAF, for example.
578
579 In the central Aegean mantle lithosphere, seismic anisotropy has been found to be small
580 (Endrun et al., 2011), consistent with this region having undergone little deformation in
581 the last 20 Myr. Our data point to the same result, where the best (and simplest) models
582 comprise only 5% of anisotropy in the upper crust (Figure 8). This is also consistent with
583 steep incident P-rays sampling only low values of anisotropy (**Fig. 7a**). It appears that
584 <5% anisotropy with a fast axis of symmetry is needed in the 20 km thick lower crustal

585 layer in order to reproduce the double polarity on the B⊥ (Figure 8). This is rather
586 unexpected, since most minerals in the upper to lower crust are well approximated by
587 hexagonal anisotropy with slow axis of symmetry. It has nonetheless been found in other
588 receiver function studies that lower crust anisotropy was best reproduced with fast axis
589 symmetry (e.g., Sherrington et al., 2004; Tian et al., 2008).
590
591 The fact that we find slow and fast symmetry axes of anisotropy suggests that the
592 meaning of the orientation α is ambiguous. Although the synthetic models find an
593 azimuth α very similar to the 80° obtained at station APE, it cannot represent the
594 orientation of both slow and fast axes at the same time, since they are shifted by 90°. A
595 test was conducted for station APE using a depth range of 7 km (corresponding to the
596 metapelite layer thickness) for the calculation of α in the harmonic decomposition. The
597 orientation obtained is 102°, which means that a slow axis of symmetry would be
598 oriented at 192° for the upper crust characterised by metapelites. This is consistent with
599 the NE-SW orientation of Miocene extension, and also with the maximum velocity and
600 anisotropy orientations calculated from EBSD data for the same rocks (Cossette et al.,
601 2015; Figure 8). It also likely explains why α varies so much across the array of stations,
602 since it depends on the proportion of anisotropy between lower and upper layers. It
603 further reinforces the notion of complex anisotropy layering in the crust as demonstrated
604 by Endrun et al. (2011). Our study shows that layering occurs at the kilometer scale.
605
606 Numerous assumptions need to be made in numerical modeling of receiver function data.
607 In these synthetic models, the anisotropy is assumed to follow a pure ellipsoid, with
608 similar percent P and S anisotropy (Porter et al., 2011). However, as calculated from
609 EBSD measurements (e.g., Lloyd et al., 2009; Bezacier et al., 2010; Bascou et al., 2001;
610 Dempsey et al., 2011; Cossette et al., 2015), very few lithotypes show pure ellipticity for
611 P- and S-waves. Blueschist, for example, has an average P-wave and S-wave anisotropy
612 of 20.3% and 14.5%, respectively. Moreover, the anisotropy in the crust is far from being
613 homogeneously distributed on a vertical profile, with layers possessing differences in
614 anisotropy as high as 20% at the km scale, depending on the orientation of the upcoming
615 P-wave (Cossette et al., 2015). There are also probably large sources of error due to the

strong dependence of the receiver functions on the Vp/Vs ratio, which varies strongly with the orientation of incoming P-waves (Cossette et al., 2015). From the resolved ray points of the P-waves and Vp/Vs plots of Cycladic rocks, we observe that the seismic rays are likely to sample the lowest values of Vp/Vs (**Fig. 7b**). Reducing the Vp/Vs ratio to 1.6-1.65 in the first 20 km of the velocity model would affect the migration results, and would lower the depth of the Moho by about 2 km. In the case of station APE, using this Vp/Vs ratio yields a more accurate Moho depth of 27 km. This demonstrates the importance of using in situ rock seismic properties oriented in the field. In fact, it is shown here that upcoming P-waves will resolve very heterogeneous values of anisotropy and Vp/Vs ratio. The good match between the calculated and synthetic receiver functions thus provides constraints on the source of seismic anisotropy in relation with in situ rock textural data, and the modeled seismic profiles confirm that we can use teleseismic receiver functions to map lateral variations in crustal structure and fabric.

Conclusion

We employed teleseismic receiver functions in the Cyclades, Greece, to constrain the layered structure and anisotropy in the crust. A Moho depth of 22.5 to 33 km with an average of 25.5 km in the south-central Aegean is found, as well as a sharp downward velocity increase at 3-11 km depth. The crust is thinner beneath the high-temperature domes of Naxos and Ios, and is thicker close to the continent. Back-azimuth harmonic decomposition points to intra-crustal anisotropy best approximated with a plunging axis of symmetry. We use two discontinuities observed at depths of 7 and 27 km at station APE to create synthetic models that include seismic properties of rocks calculated from EBSD data. Our models indicate that the upper crust is characterised by ~5% anisotropy with a slow axis of symmetry, with velocities corresponding to metapelites. Below the upper crust, a ~20 km-thick layer of dense material with high seismic velocities is needed to reproduce the observed data. Anisotropic layering is indicated both by the synthetic modeling and the harmonic decomposition, with this second layer possibly possessing 5% of anisotropy as well. Our study stresses the importance of considering in situ rock

646 textural data for seismic velocity profile interpretation, which can help map lateral
647 variations in crustal structure.
648
649 **Acknowledgements**
650
651 Python codes to calculate the receiver functions, harmonic decomposition and perform
652 receiver function modeling make extensive use of the ObsPy package developed by
653 Beyreuther et al. (2010). Funding for this research was provided by the Natural Science
654 and Engineering Research Council of Canada through Discovery grants to DAS and PA.
655 Seismic data from the GE and Z3 seismic networks were obtained from the Geofon data
656 archives (http://eida.gfz-potsdam.de/). All other data are available in the cited references.
657 We acknowledge constructive comments by two anonymous reviewers that improved this
658 paper.

References

Agostinetti, N. P., Bianchi, I., Amato A., and Chiarabba, C., 2011. Fluid migration in continental subduction: The Northern Apennines case study, Earth Planet. Sci. Lett., 302, 267–278.

Altherr, R., Kreuzer, H., Lenz, H., Wendt, I., Harre, W., and Dürr, S., 1994. Further evidence for a Late Cretaceous low-pressure/high-temperature terrane in the Cyclades, Greece; petrology and geochronology of crystalline rocks from the islands of Donoussa and Ikaria: Chem. Erde, 54, 319–328.

Andriessen, P.A.M., Banga, G., Hebeda, E.H., 1987. Isotopic age study of pre-Alpine rocks in the basal units on Naxos, Sikinos and Ios, Greek Cyclades. Geol. Mijnbouw, 66, 3-14.

Audet, P., 2010. Temporal variations in crustal velocity structure near Parkfield, California, using receiver functions, Bull. Seism. Soc. Am., 100, 1356-1362.

Audet, P., 2015. Layered crustal anisotropy around the San Andreas Fault near Parkfield, California, J. Geophys. Res., 120, 3527-3543.

Bascou, J., Barruol, G., Vauchez, A., Mainprice, D., and Egydio-Silva, M., 2001. EBSD-measured lattice-preferred orientations and seismic properties of eclogites. Tectonophysics, 342, 61– 80.

Ben Ismail, W., and Mainprice, D., 1998. An olivine fabric database: an overview of upper mantle fabrics and seismic anisotropy, Tectonophysics, 296, 145–157.

Beyreuther, M., Barsch, R., Krischer, L., Megies, T., Behr, Y., and Wassermann, J., 2010. Obspy: A Python toolbox for seismology, Seism. Res. Lett., 81, 530–533.

Bezacier, L., Reyard, B., Bass, J.D., Wang, J., and Mainprice, D., 2010. Elasticity of glaucophane, seismic velocities and anisotropy of the subducted oceanic crust. Tectonophysics, 494, 201–210.

Bianchi, I., Park, J., Agostinetti, N. P., and Levin, V., 2010. Mapping seismic anisotropy using harmonic decomposition of receiver functions: An application to Northern Apennines, Italy, J. Geophys. Res., 115, B12317, doi:10.1029/2009JB007,061.

Blake, M.C., Bonneau, M., Geyssant, J., Kienast, J.R., Lepvrier, C., Maluski, H., and Papanikolaou, D., 1981. A geological reconnaissance of the Cycladic blueschist belt, Greece: Geol. Soc. . Am. Bull., 92, 247–254.

Bohnhoff, M., Makris, J., Papanikolaou, D., Stavrakakis, G., 2001. Crustal investigation of the Hellenic subduction zone using wide aperture seismic data. Tectonophysics 343, 239-262.

Bonneau, M., 1984. Correlation of the Hellenic nappes in the south-east Aegean and their tectonic reconstruction, in The Geological Evolution of the Eastern Mediterranean, edited by J. E. Dixon and A. H. F. Robertson, pp. 517 – 527, Blackwell Sci., Oxford, U. K.

Bostock, M. G., 1998. Mantle stratigraphy and evolution of the Slave province, J. Geophys. Res., 103, B9, 21183-21200.

Bruestle, A., 2012. Seismicity of the eastern Hellenic Subduction Zone, PhD thesis, Ruhr-Universität Bochum.

Cassidy, J. F., 1992. Numerical experiments in broadband receiver function analyses, Bull. Seism. Soc. Am., 82, 1453–1474.

Cossette, É., Schneider, D., Audet, P., Grasemann, B., and Habler, G., 2015. Seismic properties and mineral crystallographic preferred orientations from EBSD data: Results from a crustal-scale detachment system, Aegean region, Tectonophysics, 651-652, 66-78.

Dempsey, E.D., Prior, D.J., Mariani, E., Toy, V.G., and Tatham, D.J., 2011. Mica-controlled anisotropy within mid-to-upper crustal mylonites: an EBSD study of mica fabrics in the Alpine Fault Zone, New Zealand. In: Prior, D.J., Rutter, E.H., Tatham, D.J. (eds) Deformation Mechanism, Rheology and Tectonics: Microstructures, Mechanics and Anisotropy. Geol. Soc., London, Special Publications 360, 33–47.

Dueker, K. G. and Sheehan, A. F., 1997. Mantle discontinuity structure from midpoint stacks of converted P to S waves across the Yellowstone hotspot track, J. Geophys. Res., 102, 8313–8327.

Dürr, S., Altherr, R., Keller, J., Okrusch, M., and Seidel, E., 1978. Themedian Aegean crystalline belt: Stratigraphy, structure, metamorphism, magmatism, in Cloos, H., Roeder, D., and Schmidt, K., eds., Alps, Apennines, Hellenides: Stuttgart, Schweizerbart, p. 455–476.

Endrun, B., Meier, T., Lebedev, S., Bohnhoff, M., Stavrakakis, G., and Harjes, H.P., 2008. S-velocity structure and radial anisotropy in the Aegean region from surface wave dispersion. Geophys. J. Int., 174, 593–616.

742 Endrun, B., Lebedev, S., Meier, T., Tirel, C., and Friederich,W., 2011. Complex layered
743 deformation within the Aegean crust and mantle revealed by seismic anisotropy. Nat.
744 Geosci. 4, 203–207.
745
746 Erdman, M., Hacker, B., Zandt, G., and Seward, G., 2013. Seismic anisotropy of the
747 crust: electron-backscatter diffraction measurements from the Basin and Range. Geophys.
748 J. Int. 195, 1211–1229.
749
750 Evangelidis, C. P., Liang, W. - T., Melis, N. S., and Konstantinou, K. I., 2011. Shear
751 wave anisotropy beneath the Aegean inferred from SKS splitting observations, J.
752 Geophys. Res., 116, B04314, doi:10.1029/2010JB007884.
753
754 Frederiksen, A.W., and Bostock, M. G., 2000. Modelling teleseismic waves in dipping
755 anisotropic structures, Geophys. J. Int., 141, 401–412.
756
757 Gautier, P. and Brun, J.P., 1994. Crustal-scale geometry and kinematics of late-orogenic
758 extension in the central Aegean (Cylades and Evvia Island), Tectonophysics, 238, 399-
759 424.
760
761 Grasemann, B., Schneider, D.A., Stöckli, D.F., Iglseder, C., 2012. Miocene bivergent
762 crustal extension in the Aegean: Evidence from the western Cyclades (Greece).
763 Lithosphere, 4, 23-39.
764
765 Hatzfeld, D., Karagianni, E., Kassaras, I., Kiratzi, A., Louvari, E., Lyon-Caen, H.,
766 Makropoulos, K., Papadimitriou, P., Bock, G., and Priestley, K., 2001. Shear wave
767 anisotropy in the upper mantle beneath the Aegean related to internal deformation, J.
768 Geophys. Res., 106, 30737-30753.
769
770 Hyndman, R.D. and Currie, C.A., 2011. Why is the North America Cordillera high? Hot
771 backarcs, thermal isostasy, and mountain belts, Geology, 39, 8, 783-786.
772
773 Jolivet, L. and Brun, J.-P., 2008. Cenozoic geodynamic evolution of the Aegean, Int. J.
774 Earth Sci., 99, 109-138.
775
776 Jolivet, L., Faccenna, C., and Piromallo, C., 2009. From mantle to crust: Stretching the
777 Mediterranean, Earth Planet. Sci. Lett., 285, 198–209.
778
779 Jolivet, L., Faccenna, C., Huet, B., Labrousse, L., Le Pourhiet, L., Lacombe, O.,
780 Lecomte, E., Burov, E., Denèle, Y., Brun, J.-P., Philippon, M., Paul, A., Salaün, G.,
781 Karabulut, H., Piromallo, C., Monié, P., Gueydan, F., Okay, A.I., Oberhänsli, R.,

782 Pourteau, A., Augier, R., Gadenne, L., Driussi, O., 2013. Aegean tectonics: Strain
783 localisation, slab tearing and trench retreat. Tectonophysics, 597–598, 1-33.
784
785 Jung, H. and Karato, S., 2001.Water-induced fabric transitions in olivine, Science, 293,
786 5534, 1460–1463.
787
788 Katzir, Y., Matthews, A., Garfunkel, Z., Schnliestdt, M., and Avigad, D., 1996. The
789 tectono-metamorphic evolution of a dismembered ophiolite (Tinos, Cyclades, Greece):
790 Geol. Mag., 133, 237–25.
791
792 Kennett, B.L.N., 1983. Seismic wave propagation in stratified media, Cambridge
793 University Press, UK, 285 pp.
794
795 Kennett, B.L.N., 1991. The removal of free surface interactions from three-component
796 seismograms, Geophys. J. Int., 104, 153-163.
797
798 Kern, H., Walther, Ch., Flüh, E. R. and Marker, M., 1993. Seismic properties of rocks
799 exposed in the POLAR profile region – constraints on the interpretation of the refraction
800 data, Precambrian Res., 64, 169-187.
801
802 Kissel, C. and Laj, C., 1988. The tertiary geodynamical evolution of the Aegean arc: a
803 paleomagnetic reconstruction, Tectonophysics, 146, 183-201.
804
805 Levin, V. and Park, J., 1997. P-SH conversions in a flat-layered medium with anisotropy
806 of arbitrary orientation, Geophys. J. Int., 131, 253-266.
807
808 Li, X., Bock, G., Vafidis, A., Kind, R., Harjes, H.-P., Hanka, W., Wylegalla, K., Meijde,
809 M.v.d., and Yuan, X., 2003. Receiver function study of the Hellenic subduction zone:
810 Imaging crustal thickness variations and the oceanic Moho of the descending African
811 lithosphere, Geophys. J. Int., 155, 733– 748.
812
813 Lister, G.S., Banga, G., Feenstra, A., 1984. Metamorphic core complexes of Cordilleran
814 type in the Cyclades, Aegean Sea, Greece. Geology, 12, 221-225.
815
816 Lloyd, G., Butler, R., Casey, M., and Mainprice, D., 2009. Mica, deformation fabrics and
817 the seismic properties of the continental crust. Earth Planet. Sci. Lett., 288, 320–328.
818
819 Makris, J., Papoulia, J., and Yegorova, T., 2013. A 3-D density model of Greece
820 constrained by gravity and seismic data, Geophys. J. Int., doi: 10.1093/gji/ggt059.
821

McDonough, D. T. and Fountain, D. M., 1988. Reflection characteristics of a mylonite zone based on compressional wave velocities of rock samples, Geophys. J. Int., 93, 547-558.

Morris, A. and Anderson, M., 1996. First palaeomagnetic results from the Cycladic Massif, Greece, and their implications for Miocene extension directions and tectonic models in the Aegean, Earth Planet. Sci. Lett., 142, 3, 397-408.

Nábělek, J., Hétenyi, G., Vergne, J., Sapkota, S., Kafle, B., Jiang, M., Chen, J., Huang, B.-S., and the Hi-CLIMB team, 2009. Underplating in the Himalaya-Tibet collision zone revealed by the Hi-CLIMB experiment, Science, 325, 1371–1374.

Nicolas, A. and Christensen, N., 1987. Formation of anisotropy in upper mantle peridotites: a review, Geodyn. Ser., 16, 111–123.

Porter, R., Zandt, G., and McQuarrie, N., 2011. Pervasive lower-crustal seismic anisotropy in Southern California: Evidence for underplated schists and active tectonics, Lithosphere, 3, 3, 201–220.

Prior, D. J., Rutter, E., and Tatham, D. J., 2011. Deformation mechanisms, rheology and tectonics: microstructures, mechanics and anisotropy: introduction. In: Prior, D.J., Rutter, E.H., Tatham, D.J. (eds) Deformation Mechanism, Rheology and Tectonics: Microstructures, Mechanics and Anisotropy. Geol. Soc., London, Special Publications 360, 33–47.

Reinecke, T., Altherr, R., Hartung, B., Hatzipanagiotou, K., Kreuzer, H., Harre, W., Klein, H., Keller, J., Geenen, E., Boger, H., 1982. Remnants of a Late Cretaceous high temperature belt on the island of Anafi (Cyclades, Greece). N. Jahrb. f. Min., 145, 157-182.

Ring, U., Layer, P.W., and Reischmann, T., 2001. Miocene high-pressure metamorphism in the Cyclades and Crete, Aegean Sea, Greece: Evidence for large-magnitude displacement on the Cretan detachment, Geology, 29, 5, 395-398.

Savage, M. K., 1998. Lower crustal anisotropy or dipping boundaries? Effects on receiver functions and a case study in New Zealand, J. Geophys. Res., 103, 15069–15087.

Sherrington, H. F., Zandt, G., and Frederiksen, A., 2004. Crustal fabric in the Tibetan Plateau based on waveform inversions for seismic anisotropy parameters, J. Geophys. Res., 109, B02312, doi:10.1029/2002JB002345.

Shiomi, K., and J. Park, 2008. Structural features of the subducting slab beneath the Kii Peninsula, central Japan: Seismic evidence of slab segmentation, dehydration and

anisotropy, J. Geophys. Res., 113, B10318, doi:10.1029/2007JB005,535.

Skarpelis, N., Tsikouras, B., and Pe-Piper, G., 2008. The Miocene igneous rocks in the basal unit of Lavrion (SE Attica, Greece): Petrology and geodynamic implications: Geol. Mag., 145, 1–15.

Sodoudi, F., Kind, R., Hatzfeld, D., Priestley, K., Hanka, W., Wylegalla, K., Stavrakakis, G., Vafidis, A., Harjes, H. P., and Bohnhoff, M., 2006. Lithospheric structure of the Aegean obtained from P and S receiver functions, J. Geophys. Res., 111, B12307, doi:10.1029/2005JB003932.

Sodoudi, F., Bruestle, A., Meier, T., Kind, R., Friederich, W. and EGELADOS working group, 2013. New constraints on the geometry of the subducting African plate and the overriding Aegean plate obtained from P receiver functions and seismicity, Solid Earth Discuss., 5, 427–461.

Thomson, C. J., 1996. Notes on waves in layered media to accompany program Rmatrix, In: Seismic waves in complex 3-D structures, Department of Geophysics, Charles University, Prague.

Tian, B.-F., Li, J. and Yao, Z.-X., 2008. Crustal anisotropy of Taihang Mountain Range using azimuthal variation of receiver functions, Acta Seismologica Sinica, 21, 4, 358-369.

Tiberi, C., Diament, M., Lyon-Caen, H., and King, T., 2001. Moho topography beneath the Corinth Rift area (Greece) from inversion of gravity data, Geophys. J. Int., 145, 797–808.

Tirel, C., Gueydan, F., Tiberi, C., and Brun, J.-P., 2004. Aegean crustal thickness inferred from gravity inversion. Geodynamical implications, Earth Planet. Sci. Lett., 228, 267–280.

Trotet, F., Jolivet, L., and Vidal, O., 2001. Tectono-metamorphic evolution of Syros and Sifnos Islands (Cyclades, Greece), Tectonophysics, 338, 179–206.

Walcott, C.R. and White, S.H., 1998. Constraints on the kinematics of post-orogenic extension imposed by stretching lineations in the Aegean region, Tectonophysics, 298, 155-175.

Worthington, J.R., Hacker, B.R. and Zandt, G., 2013. Distinguishing eclogite from peridotite: EBSD-based calculations of seismic velocities, Geophys. J. Int., 193, 489-505.

Figures

Figure 1. A: Map of the Aegean region showing seismic station locations of the GE and Z3 networks and the West and North Cycladic Detachment Systems (WCDS and NCDS). B and C: Events distribution showing the data used in this study for the permanent station APE and the temporary station SERI.

Figure 2. Receiver functions and harmonic decompositon for station APE on Naxos (A and B) and station SANT on Santorini (C and D). The azimuth α is the orientation obtained when the variance is minimised on B||. Dashed lines in A and C show the variation in arrival time for two positive velocity contrasts. Vertical red lines in A and C (horizontal red lines in B and D) indicate the average arrival time (depth) for the Moho. Black arrows indicate polarity reversals at 140° and 320° in A, and at 120° in C. Dashed circle in B refers to description in the text.

Figure 3. P-wave ray angle distribution at station APE superimposed on A: P-wave velocity (in km/s) and B: Vp/Vs ratio of metapelites in the Cyclades. The maximum and minimum velocities resolved by the P-rays are ~6.1 and ~5.9 km/s, respectively, giving a P-wave anisotropy of ~3.3%. Seismic figures are from Cossette et al. (2015) and represent data for one sample of the West Cycladic Detachment System

Figure 4. A: Diagram representing an anisotropic layer in the crust with two different orientations (models 1 and 2) and with incoming P-waves from E-W and from N-S. The orientation of B|| and B⊥ is also shown. In these models the S-wave velocity of the underlying isotropic medium is higher than the fast velocity of the anisotropic medium. B: Diagrams showing the fabric in the anisotropic layer, with its slow axis of symmetry and the orientation of the azimuth α and the back-azimuth φ for models 1 and 2. C: Plots of the SV and SH amplitudes of Ps conversions at depth h as a function of back-azimuth. Black and white dots correspond to the N-S and E-W orientation of φ, respectively, in B. For angle differences of ± 90° between φ and α, B|| is minimised / B⊥ is maximised (squared amplitude). For angle differences of 0° or 180° between φ and α, B|| is maximised / B⊥ is minimised.

Figure 5. Receiver functions for the 21 selected seismic stations of the Cyclades in function of A: time and B: depth. Dashed lines correspond to downward increase (red) and decrease (blue) in velocity. Shaded area corresponds to a possible high-velocity mantle lid below the Moho.

Figure 6. Harmonic decomposition for the 21 selected seismic stations in the Cyclades. A, C-E: harmonic components A, B||, B⊥, C|| and C⊥. Dashed lines on the term A harmonics correspond to positive velocity contrasts. Shaded areas and dashed lines on the harmonic terms B⊥ and C⊥ highlight visible trends. We note that the Moho lies in the middle of a polarity reversal on the term B⊥, best seen in the south-central Aegean. The azimuths α obtained over the 0-30 km depth range when the variance is minimal on B|| are given in B and above each trace in C.

Figure 7. A-F: Synthetic receiver functions (left) and harmonic decompositon (right) for models 1 to 6. In each radial component stack, the vertical red line shows the average arrival time of the first positive amplitudes. The black dashed line in each radial component stack traces the variation in arrival time for the first positive amplitudes according to back-azimuth. Black arrows in the transverse component stacks point to polarity reversals. Dashed boxes and circle in A, E and F refer to descriptions in the text.

Figure 8. Summary figure showing the Cyclades from the West with the crustal interface and the Moho as determined from the receiver functions. Second panel from the top shows the upper crust layer, with stretching lineations as observed in the field (e.g. Jolivet et al., 2013; Cossette et al., 2015) and the best model of anisotropy calculated with the synthetic receiver functions. Bottom figure shows the lower crust layer with the flow directions obtained from Rayleigh waves (Endrun et al., 2011) and the best model of anisotropy.

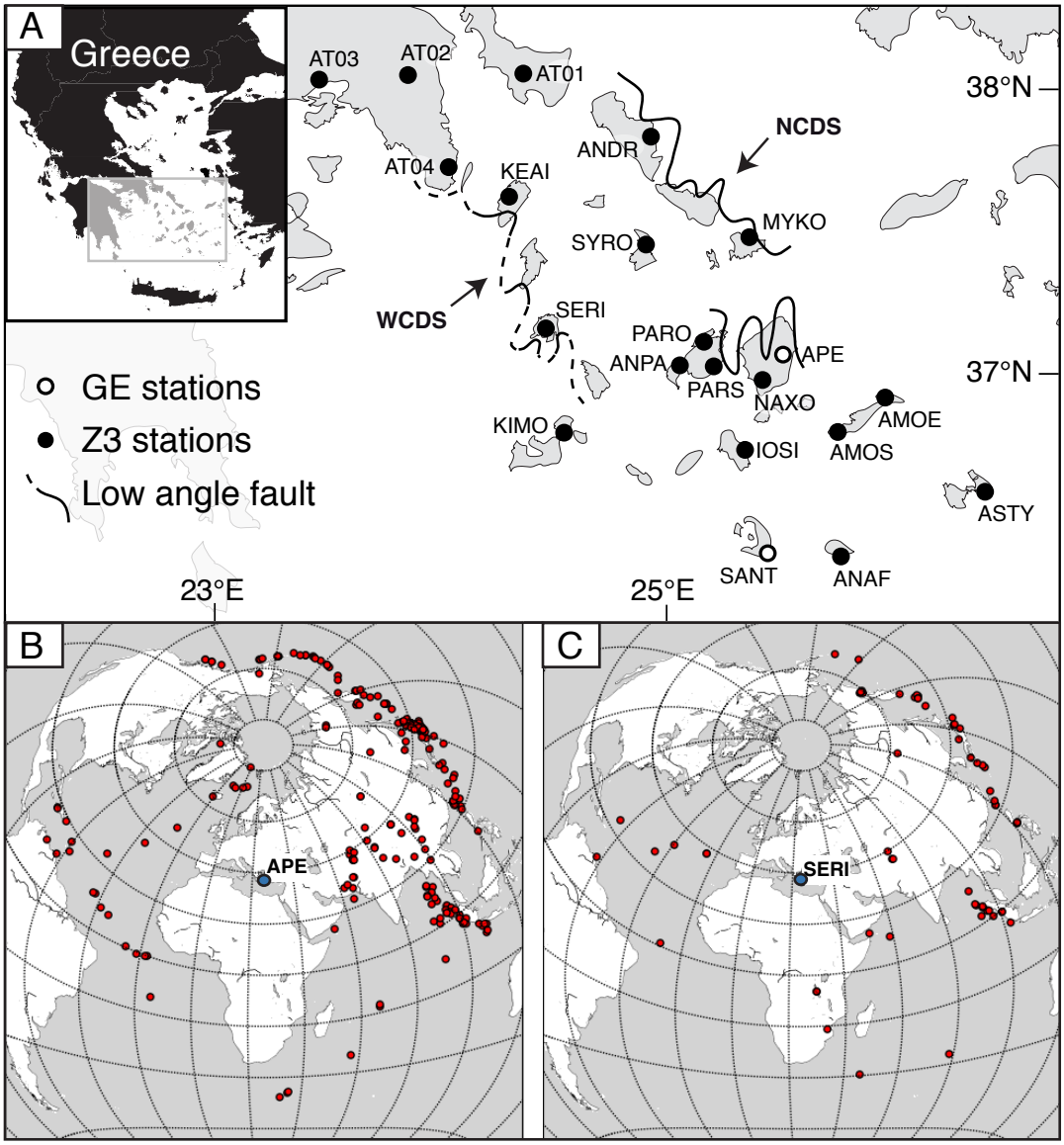
A
Greece
AT03
AT02
AT01
AT04
KEAI
ANDR
NCDS
MYKO
SYRO
WCDS
SERI
PARO
ANPA
PARS
APE
NAXO
AMOE
AMOS
KIMO
IOSI
ASTY
SANT
ANAF
38°N
37°N
23°E
25°E
GE stations
Z3 stations
Low angle fault
B
APE
C
SERI

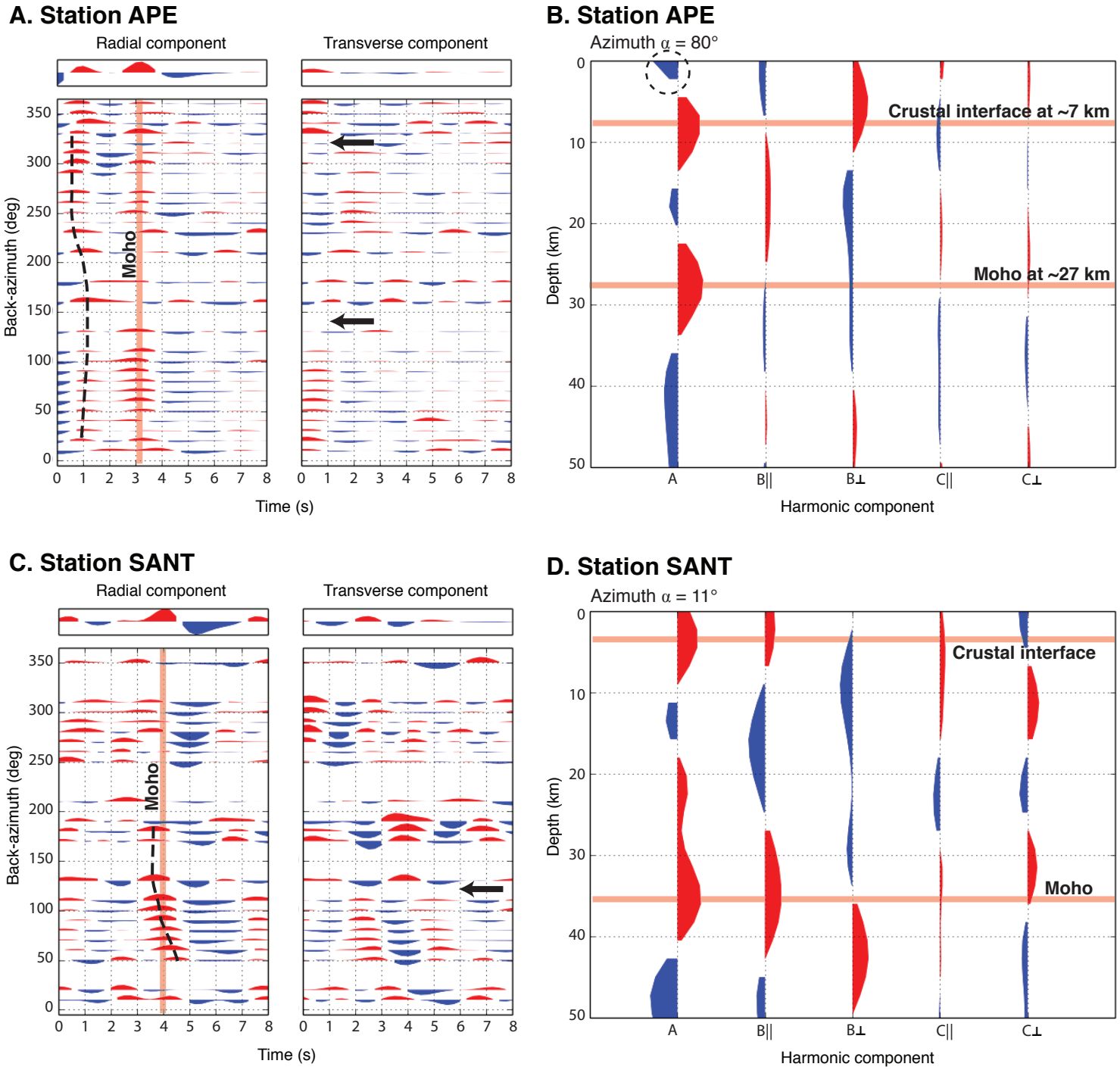
A. Station APE
Radial component
Transverse component
Back-azimuth (deg)
Moho
Time (s)
B. Station APE
Azimuth α = 80°
Crustal interface at ~7 km
Moho at ~27 km
Depth (km)
A
B||
B⊥
C||
C⊥
Harmonic component
C. Station SANT
Radial component
Transverse component
Back-azimuth (deg)
Moho
Time (s)
D. Station SANT
Azimuth α = 11°
Crustal interface
Moho
Depth (km)
A
B||
B⊥
C||
C⊥
Harmonic component

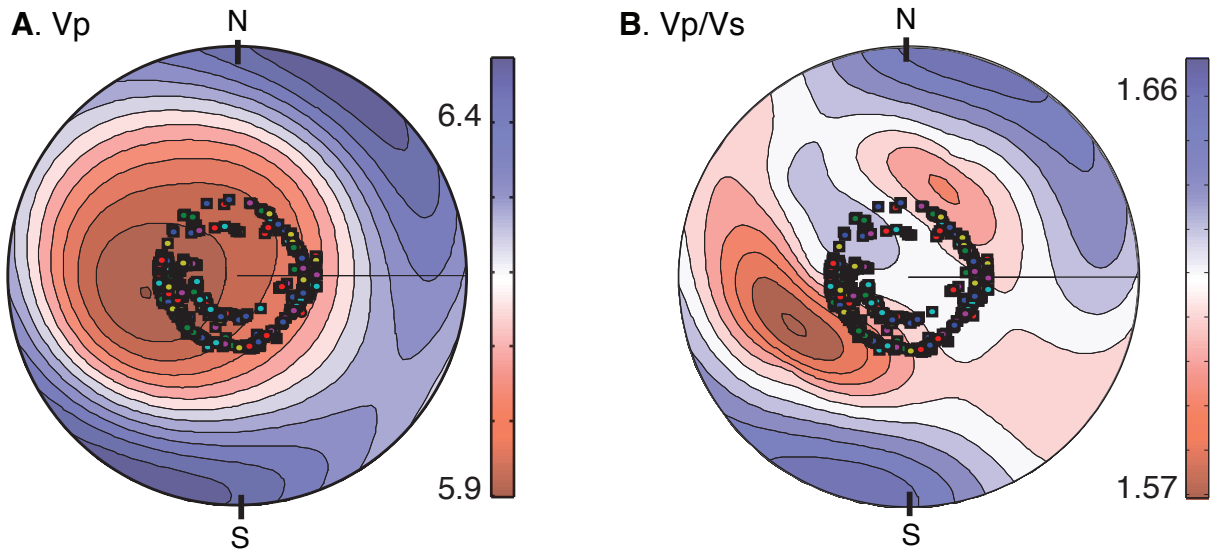
A. Vp
N
6.4
5.9
S
B. Vp/Vs
N
1.66
1.57
S

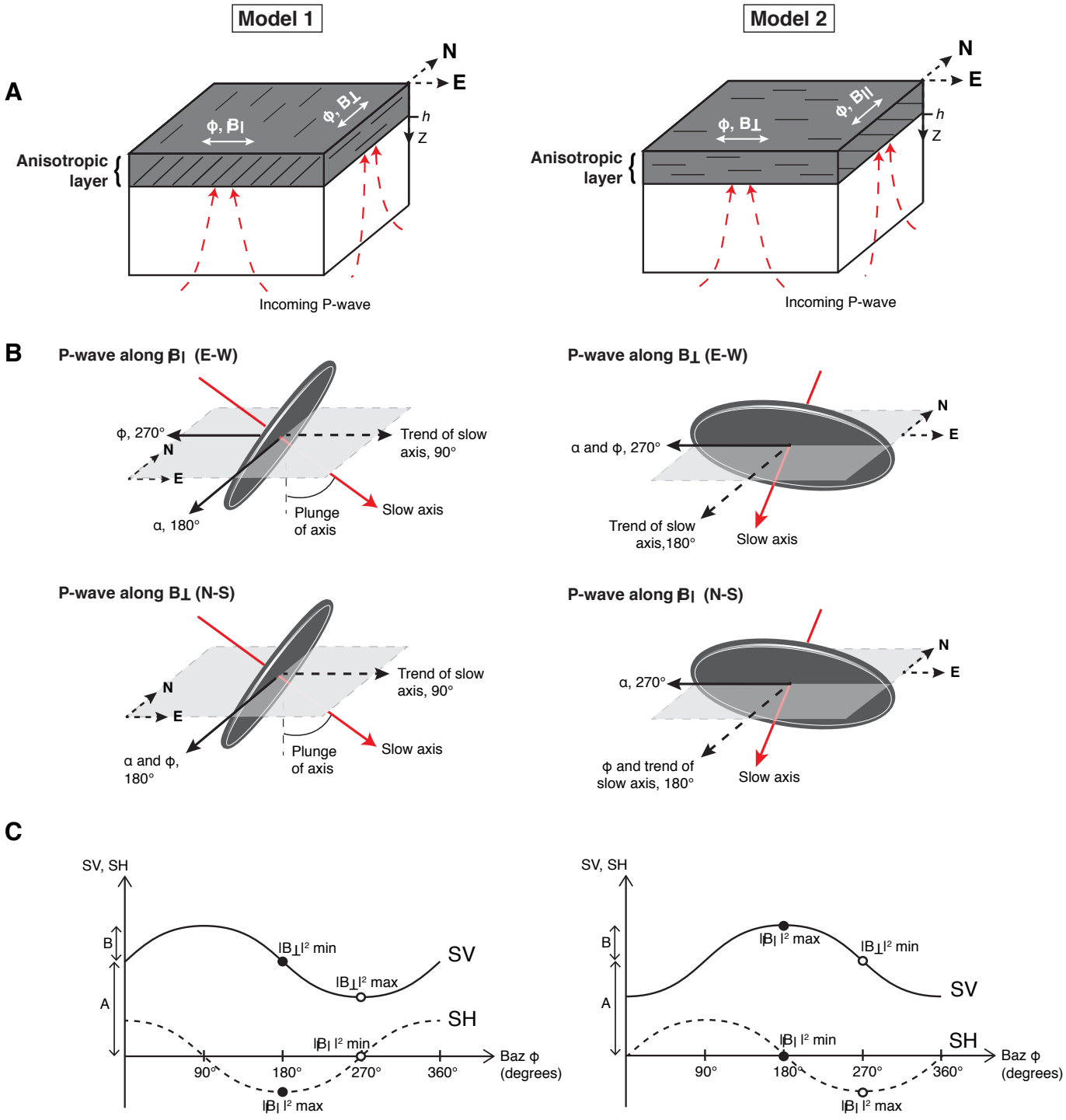
Model 1
Model 2
A
N
E
h
Z
Anisotropic layer
ϕ, B|
ϕ, B⊥
ϕ, B||
Incoming P-wave
B
P-wave along B| (E-W)
ϕ, 270°
Trend of slow axis, 90°
Plunge of axis
Slow axis
α, 180°
P-wave along B⊥ (E-W)
α and ϕ, 270°
Trend of slow axis,180°
P-wave along B⊥ (N-S)
α and ϕ, 180°
P-wave along B| (N-S)
α, 270°
ϕ and trend of slow axis, 180°
C
SV, SH
B
A
|B⊥|² min
|B⊥|² max
SV
SH
|B| |² min
|B| |² max
90°
180°
270°
360°
Baz ϕ (degrees)

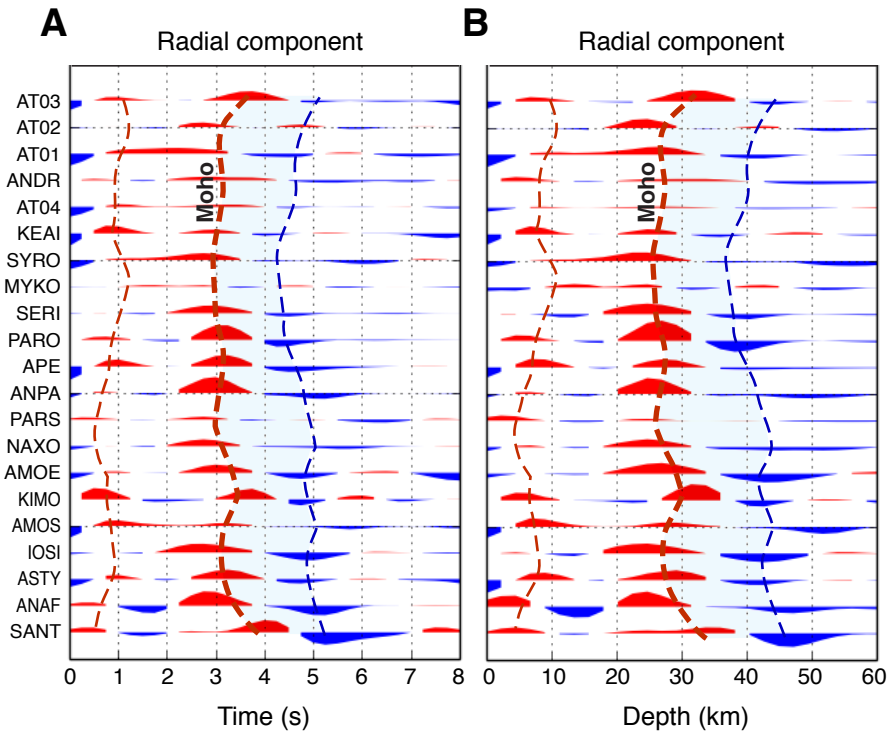
A
Radial component
B
Radial component
AT03
AT02
AT01
ANDR
AT04
KEAI
SYRO
MYKO
SERI
PARO
APE
ANPA
PARS
NAXO
AMOE
KIMO
AMOS
IOSI
ASTY
ANAF
SANT
Moho
Moho
0 1 2 3 4 5 6 7 8
Time (s)
0 10 20 30 40 50 60
Depth (km)

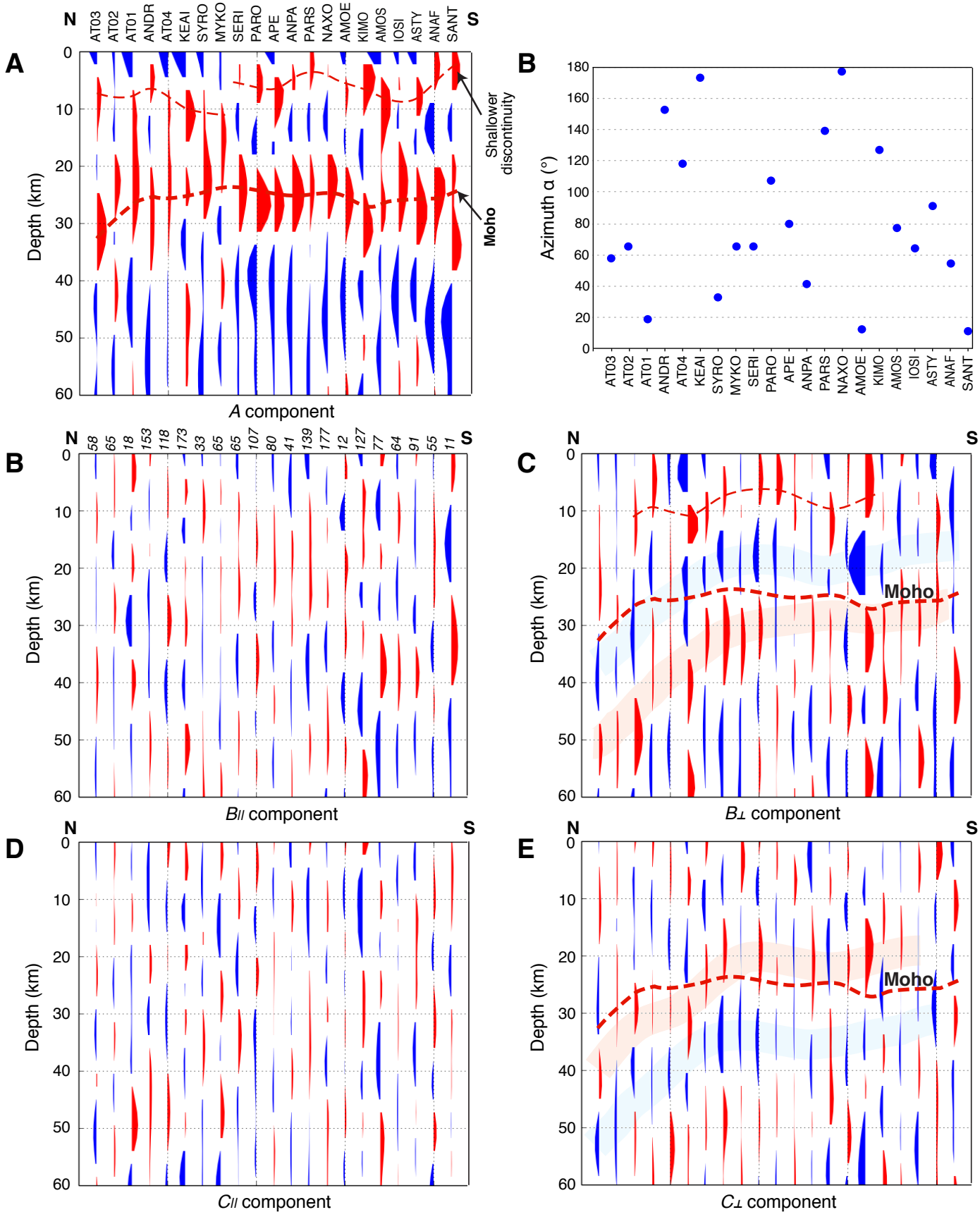
A
N
S
AT03 AT02 AT01 ANDR AT04 KEAI SYRO MYKO SERI PARO APE ANPA PARS NAXO AMOE KIMO AMOS IOSI ASTY ANAF SANT
Depth (km)
Shallower discontinuity
Moho
A component
B
Azimuth α (°)
AT03 AT02 AT01 ANDR AT04 KEAI SYRO MYKO SERI PARO APE ANPA PARS NAXO AMOE KIMO AMOS IOSI ASTY ANAF SANT
B
58 65 18 153 118 173 33 65 65 107 80 41 139 177 12 127 77 64 91 55 11
B∥ component
C
Moho
B⊥ component
D
C∥ component
E
Moho
C⊥ component

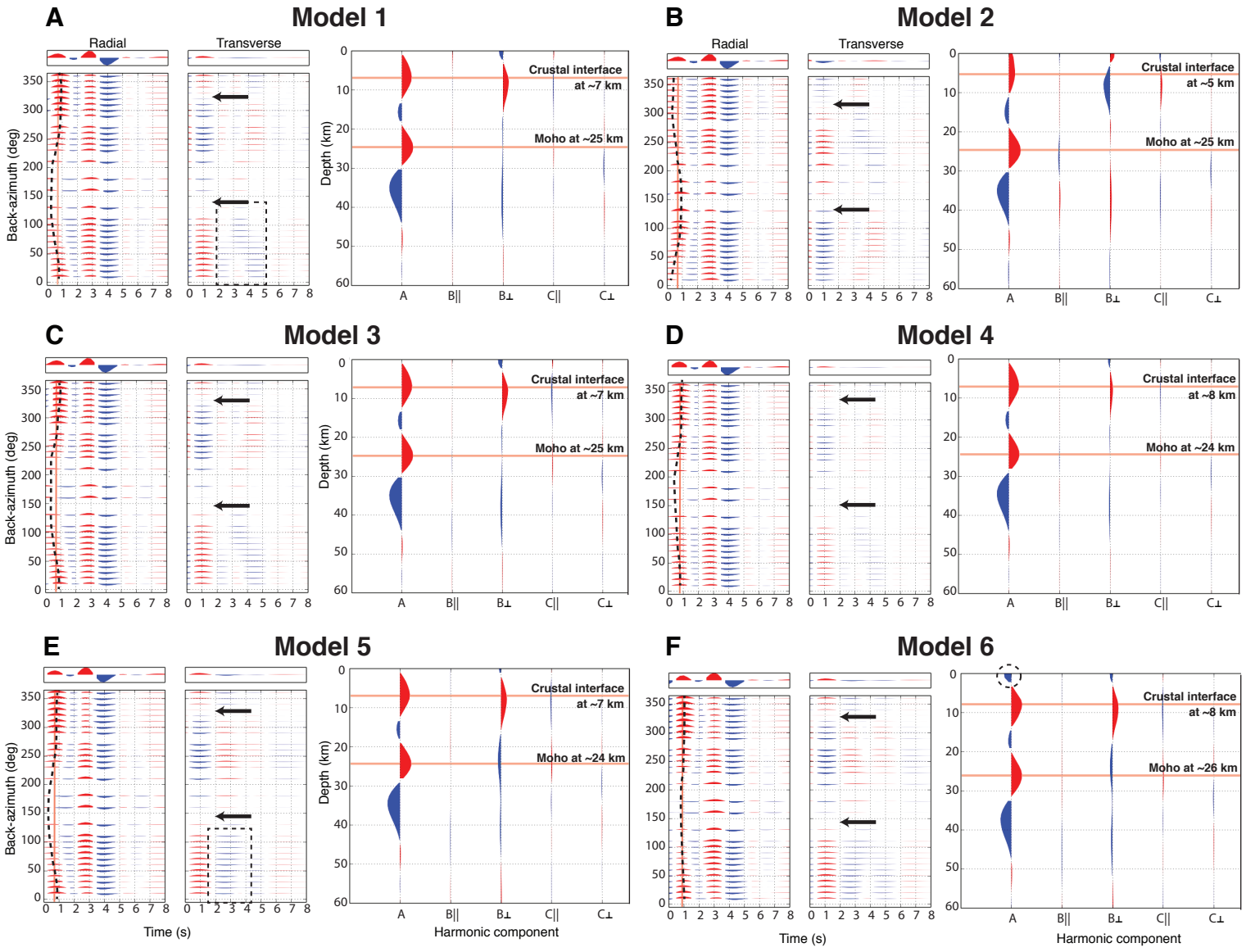
A
Model 1
Radial
Transverse
Back-azimuth (deg)
Depth (km)
Crustal interface at ~7 km
Moho at ~25 km
A
B||
B⊥
C||
C⊥
B
Model 2
Crustal interface at ~5 km
Moho at ~25 km
C
Model 3
Crustal interface at ~7 km
Moho at ~25 km
D
Model 4
Crustal interface at ~8 km
Moho at ~24 km
E
Model 5
Crustal interface at ~7 km
Moho at ~24 km
Time (s)
Harmonic component
F
Model 6
Crustal interface at ~8 km
Moho at ~26 km
Time (s)
Harmonic component

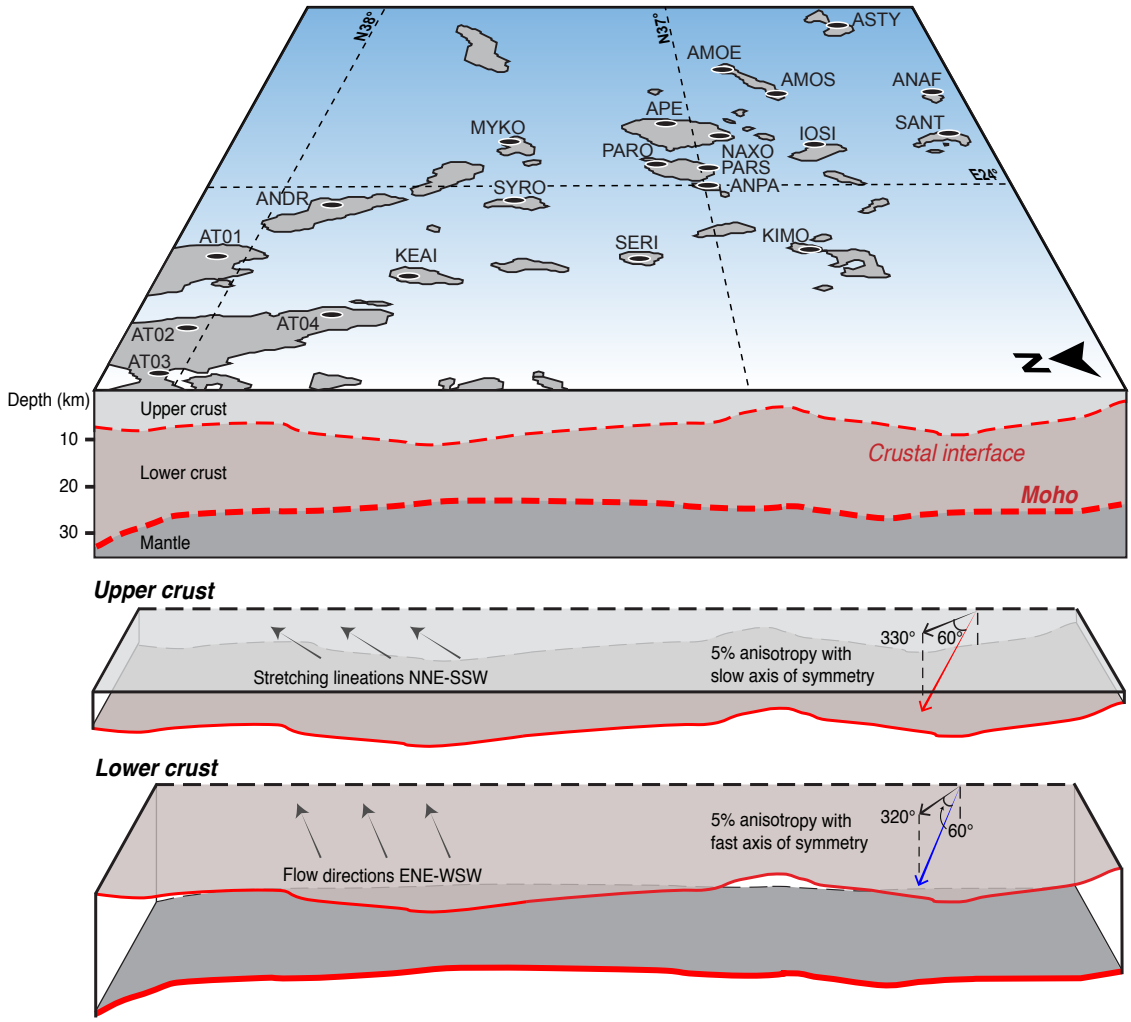
N38°
N37°
E24°
ASTY
AMOE
AMOS
ANAF
APE
SANT
MYKO
IOSI
PARO
NAXO
PARS
ANPA
SYRO
ANDR
AT01
SERI
KIMO
KEAI
AT04
AT02
AT03
N
Depth (km)
10
20
30
Upper crust
Lower crust
Mantle
Crustal interface
Moho
Upper crust
Stretching lineations NNE-SSW
5% anisotropy with
slow axis of symmetry
330°
60°
Lower crust
Flow directions ENE-WSW
5% anisotropy with
fast axis of symmetry
320°
60°

Table 1. Velocity model for the migration to depth (modified from Bruestle, 2012 and Makris et al., 2013)

Depth (km)	Vp (km/s)	Vs (km/s)	Vp/Vs
0	6	3.55	1.69
2	6.5	3.82	1.70
26	6.6	3.86	1.71
30	7.5	4.31	1.74
37	7.8	4.48	1.74
47	7.86	4.49	1.75
60	7.92	4.52	1.75
85	8.13	4.64	1.75
125	8.42	4.81	1.75
175	8.43	4.82	1.75
225	8.43	4.82	1.75

Vp values from 0 to 26 km depth are from Makris et al. (2013)
Vp values from 47 to 225 km depth are from Bruestle et al. (2012)
Vs and Vp/Vs values from 0 to 26 km depth are from Cossette et al. (2015)

Table 2. Synthetic model parameters for station APE

Model	Layer thickness (km)	Density (kg/m3)	Vp (km/s)	Vs (km/s)	% Anisotropy	Symmetry axis
1	7	2820	6.21	3.70	10	slow
	20	3250	7.50	4.40	-	-
	60	3240	7.80	4.45	-	-
2	7	2820	6.21	3.70	10	slow
	20	3250	7.50	4.40	-	-
	60	3240	7.80	4.45	-	-
3	7	2820	6.21	3.70	10	slow
	20	3250	7.50	4.40	-	-
	60	3240	7.80	4.45	-	-
4	7	2820	6.21	3.70	5	slow
	20	3250	7.50	4.40	0	-
	60	3240	7.80	4.45	0	-
5	7	2820	6.21	3.70	5	slow
	20	3250	7.50	4.40	5	fast
	60	3240	7.80	4.45	0	-
6	1	3000	7.00	3.00	5	slow
	6	2820	6.21	3.70	5	slow
	1	3050	7.00	4.00	10	slow
	19	3250	7.50	4.40	5	fast
	60	3240	7.80	4.45	0	-

Trend/plunge (deg)	Azimuth α (deg)	RMS misfit SV	RMS misfit SH	Total RMS misfit	% Increase in total RMS misfit
320/60 - -	88	9.496E-08	5.530E-08	1.099E-07	1
140/60 - -	82	9.543E-08	6.440E-08	1.151E-07	6
330/60 - -	81	9.370E-08	5.582E-08	1.091E-07	0
330/60 - -	81	9.309E-08	5.358E-08	1.074E-07	-2
330/60 320/60 -	85	9.273E-08	5.133E-08	1.060E-07	-3
330/60 330/60 330/60 320/60 -	85	7.120E-08	5.489E-08	8.990E-08	-18